IEEE Robotics and Automation Letters (RA-L) paper, presented at ICRA 2026, Vienna, Austria. Cite as RA-L paper.

Underactuated Legged-Rolling Locomotion of a Minimal Two-Rod Tensegrity Robot with Self-Recovery Capability

Yanqiu Zheng[1], Yuxuan Xiang[2], Yuetong He[2], Fumihiko Asano[2] and Isao T. Tokuda[3]

***Abstract*—A control method is proposed for a tensegrity robot to generate legged-rolling locomotion (*i.e.*, rolling movement produced by a legged system). The robot has a minimal structure composed only of two rods and four elastic cables. The difficulty of the control arises from the minimalistic structure that makes the system underactuated. Our control strategy is divided into two phases: 1) overcoming the gravitational potential energy and 2) adjusting the robot's posture to prepare for the landing. Numerical simulations demonstrated that the system was capable of traversing complex terrains with two types of gaits, *i.e.*, quasi-static and dynamic gaits. The proposed structure also enabled the robot to autonomously recover from arbitrary stationary states and initiate legged-rolling locomotion. Physical experiments validated the applicability of the tensegrity robot to various terrains such as uphill and stair climbing and showed its capability of overcoming discrete steps up to 20 % of the robot's frame length.**

***Index Terms*—Underactuated robots, Legged locomotion.**

I. Introduction

MOBILE robots are generally expected to have a capability of moving autonomously under various conditions [1]. For instance, in undeveloped or human-inaccessible critical environments, robots should be able to traverse a variety of complex terrains, and even to recover from a rollover state caused by an erratic environmental situation. Among the important capabilities required for the mobile robots are: (i) ability to traverse various terrains [2] and (ii) ability of self-recovery (*i.e.*, capability of autonomously recovering from arbitrary states and initiating locomotion without any external assistance) [3].

To address the ability (i), terrains can be roughly classified into continuous type (*e.g.*, paved roads) and discrete type (*e.g.*, undeveloped wild environments, in which changes in height take place abruptly). On continuous terrains, rolling locomotion [4], achieved by utilizing wheel-like drive units, can generally provide an efficient mobility [5]. On discrete terrains, on the other hand, legged locomotion is more suitable, *e.g.*, bipedal or quadrupedal systems that have controllable grounding points [6]–[8]. However, the legged locomotion systems are typically composed of multi-link, high-degree-of-freedom structures and are often underactuated. Thus, they require coordinated control across multiple joints to maintain balance, while generating forward locomotion.

To address the ability (ii), simple rolling systems often possess a strong capability of self-recovery because of their isotropic architecture. In contrast, in legged locomotion systems, complex control strategies are usually required to recover from failure states. This poses additional challenges under dynamic or unpredictable situations [3].

Combining the rolling locomotion and the legged locomotion can be advantageous not only for enhancing the ability to traverse various terrains [9] but also for achieving the self-recovery capability. We call such a hybrid locomotion as "legged-rolling locomotion," in which discrete grounding points are utilized for the rolling locomotion. The hybrid system may significantly improve the locomotion by enabling robots to roll over on a continuous ground and switch to legged stepping when faced with an uneven ground. Isotropic character of the rolling system may also support robots to recover from failure states. To realize such hybrid system, many existing studies base their robots on modular designs composed of multiple drive units, which allow for transitions between different locomotion modes [10]–[12]. However, utilization of the multiple drive units inevitably introduces redundant structures to the robot and consequently lowers the efficiency of its mobility. More efficient legged-rolling locomotion should be achieved by using a single drive unit, which does not require a careful design of the torso. The challenge lies in the difficulty of controlling such an underactuated system, in which full controllability over all degrees of freedom is lost due to the simplified drive unit [13].

To resolve these issues, this study proposes a minimally structured tensegrity robot [14] that can generate legged-rolling locomotion. As illustrated in Fig. 1, the robot consists only of two rigid rods and four actively controlled elastic cables, eliminating the need for torso or articulated joints. Previously, we studied passive dynamics of a slightly different tensegrity robot, and showed that various locomotion patterns can be produced in a highly energy-efficient way [15]. The applicability of the passive dynamics has been, however, limited primarily on slopes, where the gravity could be utilized as the main driving force. The present study aims to introduce underactuated control to the tensegrity robot so that it can autonomously traverse various terrains by legged-rolling locomotion.

Manuscript received: May, 15, 2025; Accepted July, 21, 2025.

This paper was recommended for publication by Editor Abderrahmane Kheddar upon evaluation of the Associate Editor and Reviewers' comments.

This work was partially supported by Grant–in–Aid for Scientific Research (No. 23K03727, No. 23H03424, No. 24K03008) from Japan Society for the Promotion of Science (JSPS).

[1]Yanqiu Zheng is with the Department of Applied Electronics Faculty of Advanced Engineering Tokyo University of Science, Niijuku 6-3-1, Katsushika, Tokyo 125-8585 Japan tei@rs.tus.ac.jp

[2]Yuxuan Xiang, Yuetong He and Fumihiko Asano are with the Graduate School of Advanced Science and Technology, Japan Advanced Institute of Science and Technology, 1-1 Asahidai, Nomi, Ishikawa 923-1292, Japan. {kouuken, s2220012 and fasano} @jaist.ac.jp

[3]Isao T. Tokuda is with the Department of Mechanical Engineering, Ritsumeikan University, 1-1-1 Nojihigashi, Kusatsu Shiga 525-8577, Japan isao@fc.ritsumei.ac.jp

Digital Object Identifier (DOI): see top of this page.

IEEE Robotics and Automation Letters (RA-L) paper, presented at ICRA 2026, Vienna, Austria. Cite as RA-L paper.

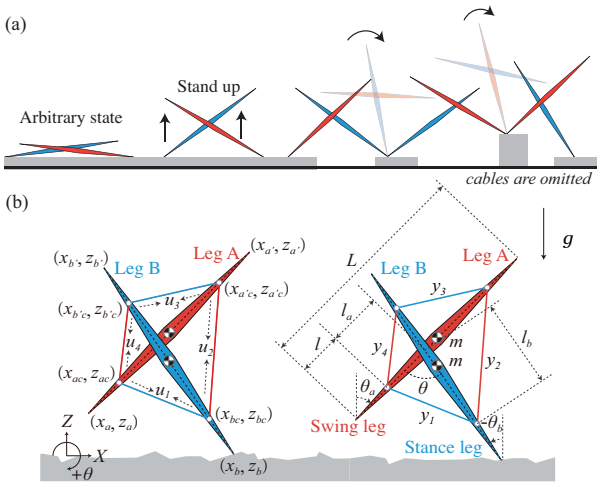

Fig. 1. Overview of proposed tensegrity robot. (a) The robot can stand up from any state and is ready for rolling locomotion. (b) Two-leg structure with four actuated cables that can be stretched/loosen by actuators through control inputs.

Important advantages of the proposed tensegrity-based structure come from its combination of lightweight design and structural compliance, which enables the legged system to absorb impact forces [16], [17]. In conventional rigid-body legged locomotion, collisions between the swing leg and the ground often result in a significant energy loss. The compliant nature of the tensegrity system reduces such impacts and realizes more energy-efficient locomotion than the corresponding rigid system. Furthermore, these structural properties enable the robot to make a transition from arbitrary postures to locomotion-ready configuration without relying on any complex control strategies. As illustrated in Fig. 1 (a), the system stands up autonomously from any state and initiate locomotion. Such self-recovery capability enhances the robustness of the system to move in a difficult environment, where rollover is inevitable.

II. MATHEMATICAL METHODS

As shown in Fig. 1 (b), the structure of the tensegrity robot is quite simple. It comprises two legs (red: swing leg A, blue: stance leg B) connected by four controllable mass-less cables. The basic parameters of the robot are listed in Table I.

This robot differs from the conventional rigid robots [18] in that, when the swing leg hits the ground, the stance leg does not immediately lift off the ground. Consequently, there is a brief period of a double-legged support phase (DLSP) followed by a single-legged support phase (SLSP). In the following subsections, equations of motions for the DLSP and SLSP are presented with the collision equation. The control method is further developed.

A. Single-legged Support Phase

Let $\boldsymbol{q} = \begin{bmatrix} x_a & z_a & \theta_a & x_b & z_b & \theta_b \end{bmatrix}^{\mathrm{T}}$ be the generalized coordinate vector. The equation of motion for the robot during the SLSP is given by:

$$\boldsymbol{M}\ddot{\boldsymbol{q}} + \boldsymbol{h} = \boldsymbol{J}_b^{\mathrm{T}}\boldsymbol{\lambda} + \boldsymbol{S}\boldsymbol{u}, \tag{1}$$

TABLE I
DEFINITION OF THE SYSTEM PARAMETERS.

Symbol	Unit	Description
$(x_i, z_i),\ i \in \{a,b\}$	m	Position of each leg
$\theta_i,\ i \in \{a,b\}$	rad	Angular position of each leg
$u_i,\ i \in [1,4]$	N	Control inputs
$y_i,\ i \in [1,4]$	m	Length of cables
l	m	Length from connection point to the tip of each leg
l_a	m	Length from (x_{ac}, z_{ac}) to the intersection of two legs
l_b	m	Length from (x_{bc}, z_{bc}) to the intersection of two legs
θ	rad	Angle between two legs
t_i and $T_i,\ i \in [1,2]$	s	Actual duration and target control period of phase i

where $\boldsymbol{M}$ is the inertia matrix, $\boldsymbol{h}$ represents the combination of central force, Coriolis accelerations, and gravity terms. On the right-hand side of Eq. (1), $\boldsymbol{J}_b$ represents Jacobian matrix for the holonomic constraints at the grounding point (x_b, z_b), and $\boldsymbol{\lambda}$ is the vector of constraint forces. The control input vector is given by $\boldsymbol{u} = \begin{bmatrix} u_1 & u_2 & u_3 & u_4 \end{bmatrix}^{\mathrm{T}}$, where $\boldsymbol{S}$ is its driving matrix.

Assuming that the grounding point does not slide on the ground as guaranteed by the static friction, the constraint equation is expressed as follows:

$$\dot{x}_b = 0, \quad \dot{z}_b = 0. \tag{2}$$

Accordingly, the constraint Jacobian matrix $\boldsymbol{J}_b$ can be summarized from Eq. (2) as:

$$\boldsymbol{J}_b\dot{\boldsymbol{q}} = \begin{bmatrix} 0 & 0 & 0 & 1 & 0 & 0 \\ 0 & 0 & 0 & 0 & 1 & 0 \end{bmatrix} \dot{\boldsymbol{q}} = \boldsymbol{0}_{2\times 1}. \tag{3}$$

By substituting the time derivative of Eq. (3) into Eq. (1), the constraint force vector $\boldsymbol{\lambda}$ can be derived as:

$$\boldsymbol{\lambda} = -\boldsymbol{X}_{bb}^{-1}\boldsymbol{J}_b\boldsymbol{M}^{-1}(\boldsymbol{S}\boldsymbol{u} - \boldsymbol{h}), \tag{4}$$

where $\boldsymbol{X}_{bb} := \boldsymbol{J}_b\boldsymbol{M}^{-1}\boldsymbol{J}_b^{\mathrm{T}}$.

B. Double-legged Support Phase

During the DLSP following the collision, the grounding points of the robot, (x_a, z_a) and (x_b, z_b), remain fixed. The equation of motion can be expressed as follows:

$$\boldsymbol{M}\ddot{\boldsymbol{q}} + \boldsymbol{h} = \boldsymbol{J}_a^{\mathrm{T}}\boldsymbol{\lambda}_a + \boldsymbol{J}_b^{\mathrm{T}}\boldsymbol{\lambda}_b + \boldsymbol{S}\boldsymbol{u}, \tag{5}$$

where $\boldsymbol{\lambda}_a$ and $\boldsymbol{\lambda}_b$ are constraint force vectors associated with the contact points (x_a, z_a) and (x_b, z_b), respectively.

In a similar manner as solving $\boldsymbol{\lambda}$ in Eq. (4), $\boldsymbol{\lambda}_a$ and $\boldsymbol{\lambda}_b$ are derived as follows:

$$\boldsymbol{\lambda}_a = -\boldsymbol{X}_{aa}^{-1}\boldsymbol{J}_a\boldsymbol{M}^{-1}(\boldsymbol{S}\boldsymbol{u} - \boldsymbol{h}), \tag{6}$$

$$\boldsymbol{\lambda}_b = -\boldsymbol{X}_{bb}^{-1}\boldsymbol{J}_b\boldsymbol{M}^{-1}(\boldsymbol{S}\boldsymbol{u} - \boldsymbol{h}) = \boldsymbol{\lambda}. \tag{7}$$

Here, the state transition from DLSP to SLSP is detected when the vertical ground reaction force of the rear leg decreases to zero while the front one remains positive.

IEEE Robotics and Automation Letters (RA-L) paper, presented at ICRA 2026, Vienna, Austria. Cite as RA-L paper.

C. Collision Equation

Assuming that the ground is rigid enough, the equations of inelastic collision can be written as:

$$\boldsymbol{M}\dot{\boldsymbol{q}}^{+} = \boldsymbol{M}\dot{\boldsymbol{q}}^{-} + \boldsymbol{J}_I^{\mathrm{T}}\boldsymbol{\lambda}_I, \tag{8}$$

$$\boldsymbol{J}_I\dot{\boldsymbol{q}}^{+} = \boldsymbol{0}_{2\times 1}, \tag{9}$$

where the superscripts "−" and "+" denote the states immediately before and after the collision, respectively. By simultaneously solving Eqs. (8) and (9), we obtain $\dot{\boldsymbol{q}}^{+}$ as:

$$\dot{\boldsymbol{q}}^{+} = \left(\boldsymbol{I}_6 - \boldsymbol{M}^{-1}\boldsymbol{J}_I^{\mathrm{T}}\boldsymbol{X}_I^{-1}\boldsymbol{J}_I\right)\dot{\boldsymbol{q}}^{-}, \tag{10}$$

where $\boldsymbol{X}_I := \boldsymbol{J}_I\boldsymbol{M}^{-1}\boldsymbol{J}_I^{\mathrm{T}}$. $\boldsymbol{J}_I = \boldsymbol{J}_{a'}$ refers to the point of collision being at the opposite tip of swing leg A.

D. Control Method

The dynamics of the tensegrity system is driven by the four cables, which interconnect the two legs. This subsection develops a method to control the length of the four cables. As shown in Fig. 1, the two legs are connected to the four cables at four points. At each connection point, two cables apply two forces to the corresponding leg. Thus, the control inputs in Eq. (1) are expressed as:

$$\boldsymbol{S}\boldsymbol{u} = \sum_{i=1}^{8}\boldsymbol{J}_i^{\mathrm{T}}\boldsymbol{F}_i, \tag{11}$$

using the Jacobian matrix $\boldsymbol{J}_i$. The force vector $\boldsymbol{F}_i$ ($i = 1,2,\ldots,8$) is composed of eight forces generated by the four cables acting on the connection points in counterclockwise order starting from (x_{ac}, z_{ac}).

Taking the first component of the control inputs $\boldsymbol{J}_1^{\mathrm{T}}\boldsymbol{F}_1$ as an example, it can be expressed as:

$$\boldsymbol{J}_1^{\mathrm{T}}\boldsymbol{F}_1 = \boldsymbol{J}_1^{\mathrm{T}}\boldsymbol{d}_{acbc}u_1, \tag{12}$$

where

$$\boldsymbol{J}_1 = \boldsymbol{J}_{ac} = \begin{bmatrix} 1 & 0 & \cos\theta_a & 0 & 0 & 0 \\ 0 & 1 & -\sin\theta_a & 0 & 0 & 0 \end{bmatrix}, \tag{13}$$

and $\boldsymbol{d}_{acbc}$ represents the direction vector from (x_{ac}, z_{ac}) to (x_{bc}, z_{bc}).

As shown in Fig. 1, the length of the four cables $\boldsymbol{y}$ are expressed by using three parameters, l_a, l_b, and θ, as:

$$\boldsymbol{y} := \begin{bmatrix} y_1 \\ y_2 \\ y_3 \\ y_4 \end{bmatrix} = \begin{bmatrix} \sqrt{l_a^2 + l_b^2 - 2l_a l_b\cos\theta} \\ \sqrt{l_b^2 + \hat{l}_a^2 - 2l_b\hat{l}_a\cos(\pi-\theta)} \\ \sqrt{\hat{l}_a{}^2 + \hat{l}_b^2 - 2\hat{l}_a\hat{l}_b\cos\theta} \\ \sqrt{l_a^2 + \hat{l}_b^2 - 2l_a\hat{l}_b\cos(\pi-\theta)} \end{bmatrix}, \tag{14}$$

where $\hat{l}_a := L - 2l - l_a$ and $\hat{l}_b := L - 2l - l_b$. Note that this also provides a geometric constraint condition for the robot to form a reasonable posture.

To achieve any desired posture determined by the vector $\boldsymbol{y}$, which must satisfy the constraint condition of Eq. (14), the desired trajectory can be represented by a fifth-order function of time as:

$$\boldsymbol{y}_d(t) = \begin{cases} \sum_{k=0}^{5} a_k t^k & \text{for} \quad 0 < t \leqslant T, \\ \sum_{k=0}^{5} a_k T^k & \text{for} \quad t > T, \end{cases} \tag{15}$$

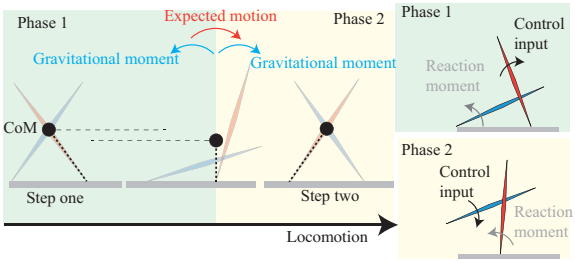

Fig. 2. Control strategy for quasi-static gait. Two-phase motion overcoming potential barriers and stabilizing landing.

where T is the target control period, until which the desired posture is achieved. In the following section, the control periods for phase 1 and phase 2 are denoted as T_1 and T_2, respectively. For a smooth connection between the two phases, initial state of the desired trajectory was set to match the robot's current state, while the target velocity and acceleration at the desired position were set to zero.

Towards achieving $\boldsymbol{y} \to \boldsymbol{y}_d$, the feedback control inputs $\boldsymbol{u}$ can be determined as:

$$\boldsymbol{u}(t) = \max\left\{\boldsymbol{0}, -K_P(\boldsymbol{y}_d(t) - \boldsymbol{y}(t)) - K_D(\dot{\boldsymbol{y}}_d(t) - \dot{\boldsymbol{y}}(t))\right\}. \tag{16}$$

A simple PD control was used with the gains K_P and K_D set to 10000 and 100 for all simulations. As the cables can only provide tension, negative control inputs should be avoided.

III. SIMULATION RESULTS

This section develops two control strategies for the tensegrity robot to generate legged-rolling locomotion.

A. Control Strategies

The control of underactuated legged locomotion is divided into two distinct phases (Fig. 2). Phase 1 aims at overcoming the gravitational potential energy barrier to initiate the movement, while phase 2 adjusts the robot's posture to prepare for the landing and to move on to the next locomotion step [19]. The proposed control method produces two types of gaits, *i.e.*, quasi-static gait and dynamic gait. The quasi-static gait, which can initiate from a stationary posture, is ideal for navigating complex terrains by prioritizing stability over speed, while the dynamic gait maximizes efficiency and velocity, and can generate a limit cycle gait with an appropriate initial velocity.

B. Quasi-static Gaits

As the basic type of legged-rolling locomotion, quasi-static gaits were simulated. The parameter values were set to $(m, I, L, l) = (1.5,\ 2m(L/2)^2,\ 0.5,\ 0.1)$, whereas the initial condition was set to $l_a(0) = l_b(0) = (L-2l)/2$, $\theta(0) = \pi/2$, which represents a cross-legged posture. These parameter values were chosen because they provided a well-balanced posture. Other parameter settings should work as well.

To study basic properties of the control method, phases 1 and 2 were examined separately. In phase 1, the control period T_1 and the target angle $\theta(T_1)$ are crucial in overcoming the gravitational potential energy barrier, moving the robot's center of mass (CoM) to a forward direction. The control target

IEEE Robotics and Automation Letters (RA-L) paper, presented at ICRA 2026, Vienna, Austria. Cite as RA-L paper.

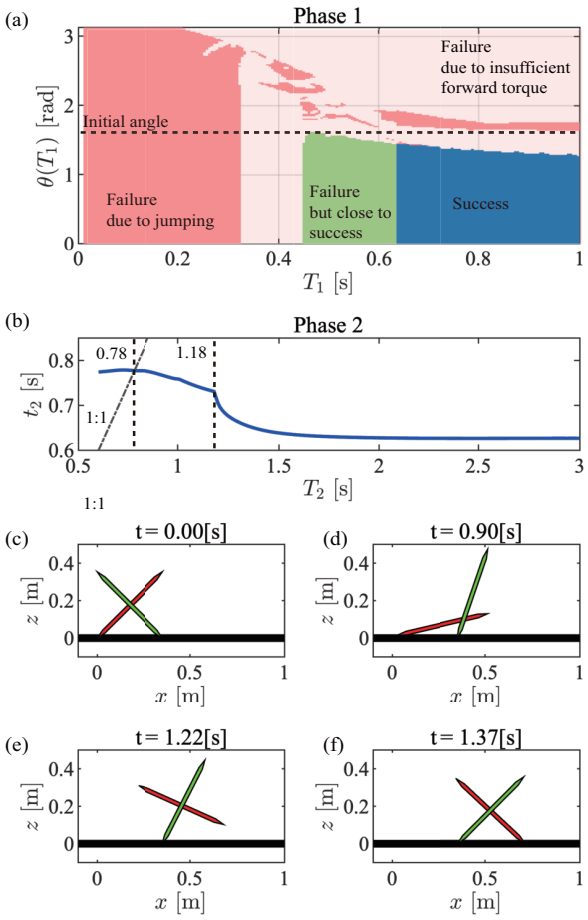

Fig. 3. (a) Dependence of the outcome of phase 1 on the varied control parameters $T_1 \in [0\ \text{s}, 1\ \text{s}]$ and $\theta(T_1) \in [0\ \text{rad}, \pi\ \text{rad}]$. (b) Dependence of the phase 2 duration t_2 on the control period T_2. (c-f) Animated sequences illustrate a complete step of quasi-static gait. Images of (c-d) and (e-f) represent phase 1 and phase 2, respectively.

at the end of phase 1 was set to $(l_a(T_1), l_b(T_1)) = (L-2l,\ 0)$, where $l_a(T_1)$ and $l_b(T_1)$ reach their maximum and minimum, respectively. As shown in Fig. 3(d), this configuration minimized the height of CoM and reduced the energy barrier.

To examine the condition, under which phase 1 overcomes the potential energy barrier, the control parameters were varied in the range of $T_1 \in [0.01\ \text{s}, 1\ \text{s}]$ and $\theta(T_1) \in [0\ \text{rad}, \pi\ \text{rad}]$. The results are summarized in Fig. 3(a), where different color regions represent different outcomes.

- Dark blue region: The robot crossed the potential energy barrier successfully.
- Light red region: The robot failed to overcome the potential energy barrier due to insufficient forward torque, which could be attributed to two main factors: 1) insufficient energy input and 2) excessive input leading to a jumping motion that compromised the generation of effective forward torque.
- Dark red region: Because of excessive input power, the robot jumped from the ground and fell upon landing.
- Green region: In a similar manner as the dark red region, the robot jumped from the ground. However, since the jumping height was relatively small, the robot successfully crossed the potential barrier. Although it was successful, the jump introduced a significant amount of uncertainty in the locomotion stability. This outcome was therefore considered a failure.

Also, the dashed line represents the initial angle between the two legs $\theta(0)$. All successful gaits are located below this dashed line, indicating that decreasing θ during phase 1 supported the crossing of the potential energy barrier. This provides a guideline for setting the parameters. In addition, all successful gaits were observed in the region, where the control period T_1 is set to be long enough. Such a long T_1 made the target trajectory smooth, required less amount of acceleration, and consequently avoided excessive amount of input power, which could lead to jumping of the robot from the ground.

Next, phase 2 was examined by varying the control period T_2. In phase 2, the initial state was given by the final state of phase 1. Thus, the target state of the phase 1, *i.e.*, $(l_a(T_1),\ l_b(T_1),\ \theta(T_1)) = (L-2l,\ 0,\ 1.3)$, was used as the initial condition of phase 2. To simulate a non-ideal starting condition, an initial kinetic energy of $\dot{\theta}_a(0) = 0.5$ was introduced, which increased the difficulty of control. To quantify the performance of phase 2, the duration t_2, at which phase 2 was completed by the landing of the swing leg on the ground, was measured.

Fig. 3(b) shows dependence of the phase 2 duration t_2 on the control period T_2. For a very short control period, *i.e.*, $T_2 < 0.6$ s, no curve was drawn because phase 2 was not successful. Here, an excessively large backward momentum of stance leg was produced, causing the robot to fall backward. For $T_2 > 0.6$ s, the phase 2 was all successful. In the region of $0.6\text{s} < T_2 < 0.78\text{s}$, the phase 2 duration t_2 exceeded the control period (*i.e.*, $t_2 > T_2$), meaning that the posture reached the target before the landing. Since the target posture matches the initial posture of the following phase 1, the robot can immediately start the next step. This is therefore an ideal region. As the control period T_2 became longer than 0.78 s, the phase 2 duration t_2 became smaller than the control period (*i.e.*, $t_2 < T_2$), where the robot did not reach the target posture before the landing. This region is not ideal because, after the landing, the robot must adjust its posture to prepare for the next step. As the control period T_2 exceeded 1.18 s, the motion duration dropped abruptly and converged towards 0.63 s, suggesting a significant decrease in the effectiveness of the control. Here, it took a longer time for the robot to adjust its posture after the landing.

Finally, phases 1 and 2 were combined to produce a complete step of quasi-static gait. Fig. 3(c-f) displays a successful example with animated images (the cables are omitted). The control parameters were set to $(l_a(T_1),\ l_b(T_1),\ \theta(T_1),\ T_1) = (0.95(L-2l),\ 0.04(L-2l),\ \pi/3,\ 0.86)$ for phase 1 and $T_2 = 0.44$ for phase 2. The initial and final states were set to the cross-legged posture. Starting from a static posture (a), the robot reached to the state which crossed the potential energy barrier (b), completing phase 1. In phase 2, the posture was adjusted (c) and the system landed on the ground (d), where deviation from the target landing position was only 0.0034 m and the locomotion speed was 0.26 m/s.

C. Dynamic Gaits

In dynamic gait, the control does not require the robot to precisely reach a specific position at each phase. Phase 1 was

IEEE Robotics and Automation Letters (RA-L) paper, presented at ICRA 2026, Vienna, Austria. Cite as RA-L paper.

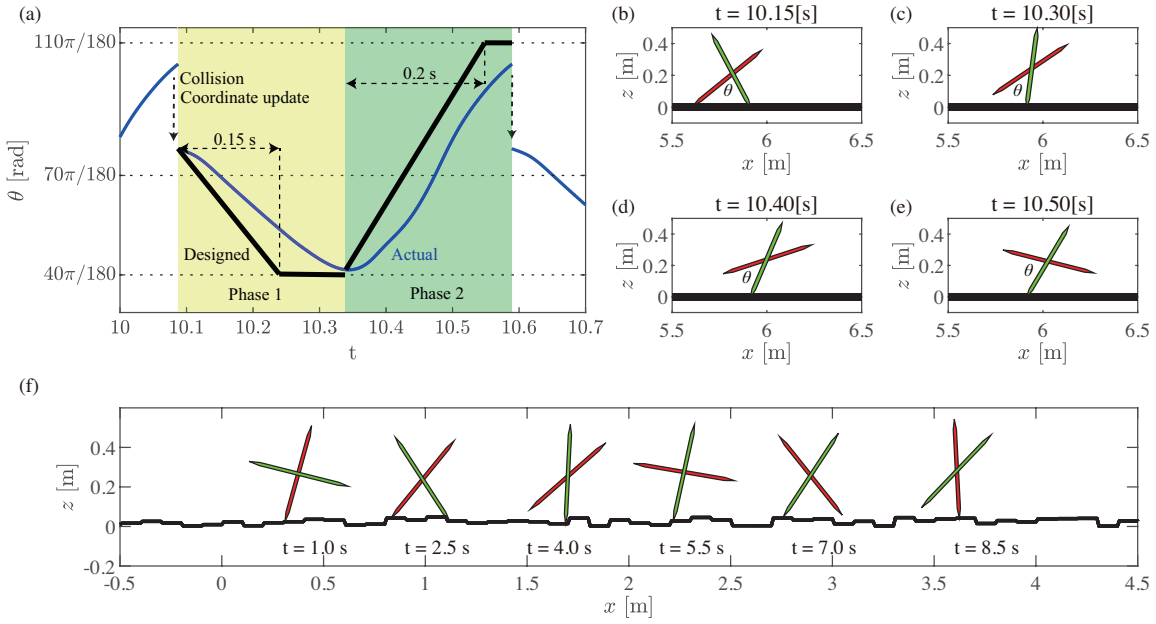

Fig. 4. Simulation results of dynamic gait. (a) Time course of angle θ between the two legs. (b-e) Animated sequences of a complete step, where (b,c) and (d,e) correspond to phases 1 and 2, respectively. (f) Successful dynamic legged-rolling gait on uneven terrain.

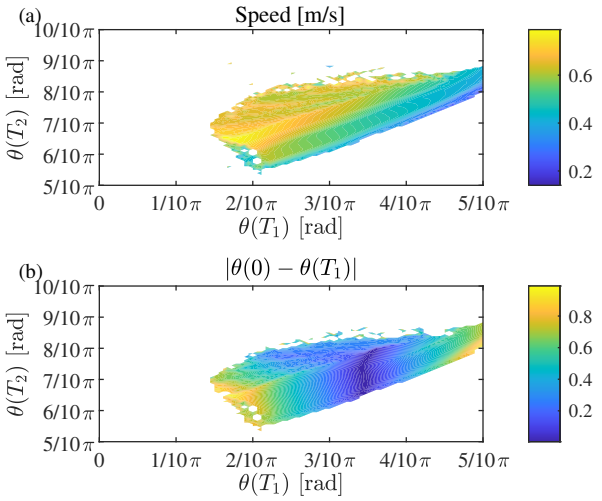

Fig. 5. Influence of target angle positions $\theta(T_1)$ and $\theta(T_2)$ on dynamic gait. Colors represent the average speed in (a) and mismatch between the initial and target angles of phase 1 $|\theta(0)-\theta(T_1)|$ in (b).

terminated at the point where the robot crossed the potential barrier, whereas phase 2 was terminated at the point where the swing leg landed on the ground. Fig. 4(a-e) shows an example of dynamic gait. The specific parameters were set as follows:

- Phase 1: $l_a(T_1) = l_b(T_1) = (L-2l)/2$, $\theta(T_1) = 40\pi/180$, $T_1 = 0.15$.
- Phase 2: $l_a(T_2) = l_b(T_2) = (L-2l)/2$, $\theta(T_2) = 110\pi/180$, $T_2 = 0.2$.

Since the target states for l_a and l_b were set to be the same for phases 1 and 2, the leg lengths to the intersection of two legs was controlled to be the same throughout the gait. The angle θ was controlled to start from 70° (= 180° − 110°) (*i.e.*, final state of phase 2), reach to 40° (*i.e.*, final state of phase 1), and return to 110° (*i.e.*, final state of phase 2). Fig. 4(b-e) shows animated images for one step of the dynamic gait. In phase 1, the target angle θ reached 40° within 0.15 s, using forward momentum of the stance leg. Then, by maintaining its target posture, the robot overcame the gravitational potential energy barrier. In phase 2, the angle θ was increased from 40° to 110° to prepare for the landing.

Fig. 4(a) shows a time trace of angle θ during a single locomotion step, corresponding to Fig. 4(b-e). The blue line represents the actual trajectory, while the black line indicates the target trajectory defined by the control parameters of phases 1 and 2. As soon as the previous step was completed by the swing leg which landed on the ground, the system updated its coordinates (*i.e.*, $\theta_{new} = \pi - \theta_{previous}$), resulting in a position jump. Then the system moved towards 40°. Phase 1 was finished when the robot overcame the potential barrier. As phase 2 started, the robot followed a new trajectory until the swing leg landed on the ground.

Fig. 4(f) shows animated images of dynamic gait on uneven terrain. The surface level varied randomly in the range from -0.025 m to 0.025 m, which corresponds to 10 % of the robot's frame length.

To study how the dynamic gait depends upon the control parameters, the robot was simulated by varying the target angle positions, $\theta(T_1)$ and $\theta(T_2)$. The results are shown in Fig. 5(a), where the color represents the locomotion speed averaged over 10 s. Overall, the speed was much higher than that of the quasi-static gait of Fig. 3(c-f). In particular, high-speed gaits were observed on the upper-left corner of the successful walking region (*i.e.*, small $\theta(T_1)$ and large $\theta(T_2)$). In the middle of this region, the highest speed appeared around $\theta(T_1) = 1.8/10\pi$ and $\theta(T_2) = 6.5/10\pi$. This peak performance was robust in the sense that slight changes in $\theta(T_1)$ and $\theta(T_2)$ did not alter the stable locomotion.

Finally, to realize dynamic gait in a real robot, simplified control is of crucial importance. In the present approach, the posture has been changed to achieve the corresponding target

IEEE Robotics and Automation Letters (RA-L) paper, presented at ICRA 2026, Vienna, Austria. Cite as RA-L paper.

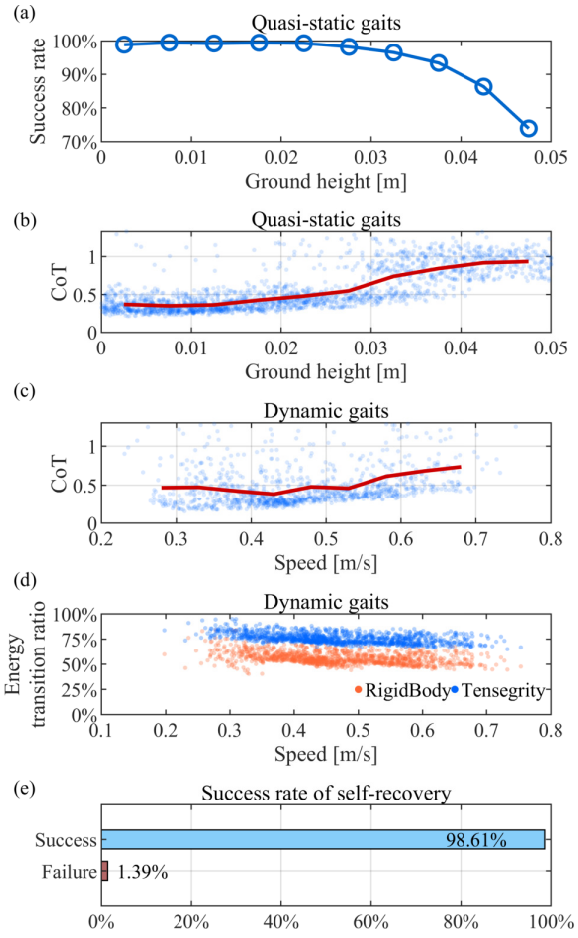

Fig. 6. Performance evaluation of the tensegrity robot with random simulations. (a) Success rate of quasi-static gaits under various step heights. (b) CoT corresponding to (a). (c) CoT for dynamic gaits at different locomotion speeds. The red lines in (b) and (c) represent averaged values over the scattered data points. (d) Comparison of energy transition ratio between tensegrity (blue) and rigid-body structures (orange). (e) Success rate of self-recovery under various initial postures.

in both phases 1 and 2. If phase 1 does not require any posture change, the control becomes simple. Such control becomes possible if the initial and target angles of phase 1 coincide with each other (*i.e.*, $\theta(0) = \theta(T_1)$). To explore the control parameters satisfying this condition, mismatch between the initial and target angles of phase 1 was calculated as $|\theta(0) - \theta(T_1)|$ in Fig. 5(b). There exists a region around $\theta(T_1) = 3.5/10\pi$ and $\theta(T_2) \in [6.5/10\pi, 8/10\pi]$, where the mismatch was very close to zero. These parameter configurations can be used to simplify the control process, in which the robot's posture remains unchanged during phase 1. Such control strategy plays a key role in the next experimental study.

D. Performance Evaluation

To evaluate the system performance, quasi-static gaits were simulated on discrete steps for 10^4 sets of randomly selected parameter values. The step height was varied in the range of $z_{\text{ground}} \in [0, 0.05]$. As the initial condition, one foot was positioned at $(0, 0)$, while the other was positioned in the range of $x_{\text{ground}} \in [0.21, 0.24]$. The initial angle θ was set in such a way that the CoM was located at the highest position. The control parameters were set as $l_a(T_1) = l_b(T_1) = (L - 2l)/2$, $\theta(T_1) \in [10\pi/180, 0.9\theta]$, $T_1 \in [0.2, 0.4]$. Fig. 6(a) shows the success rate of the quasi-static gait. For small step heights, the success rate was very high and it decreased gradually as the step height was increased. In Fig. 6(b), the cost of transport (CoT) was evaluated as $\text{CoT} = E/(mgp_{\mathbf{CoM}})$, where E and $p_{\mathbf{CoM}}$ represent input energy and displacement of the CoM, respectively. As the step height was increased, the CoT tended to increase. For a step height up to 0.025 m, the average CoT was below 0.5, indicating that highly efficient gait were realized [20], [21].

In addition to quasi-static gaits, dynamic gaits were also simulated on a level ground for randomly selected control parameters: $\theta(T_1) \in [0, 0.5\pi]$, $\theta(T_2) \in [0.5\pi, \pi]$, $T_1 \in [0.2, 0.4]$, $T_2 \in [0.2, 0.4]$. Fig. 6(c) shows the dependence of the CoT on the locomotion speed. Again the averaged CoT was below 0.5 for speed lower than 0.5 m/s. The fact that the locomotion speed did not significantly increase the CoT implies that the tensegrity structure absorbed the impact of reaction forces from the ground. To validate this feature, the energy transition ratio was computed as E_k^+/E_k^-, where $E_k^- = \dot{\boldsymbol{q}}^{-\mathrm{T}}\boldsymbol{M}\dot{\boldsymbol{q}}^-/2$ and $E_k^+ = \dot{\boldsymbol{q}}^{+\mathrm{T}}\boldsymbol{M}\dot{\boldsymbol{q}}^+/2$ represent the kinetic energies before and after the collision. As shown in Fig. 6(d), the energy transition ratio of the tensegrity system was much higher than that of the corresponding rigid-body system, indicating that the energy loss was indeed minimized by the tensegrity structure.

Fig. 6(e) shows the simulation results of evaluating the self-recovery capability of the robot from 10^4 sets of random initial postures. In each simulation, the robot changed its posture from a random configuration, in which the two rods were arbitrarily crossed, to the cross-legged configuration defined previously. A trial was considered failure if the robot was unable to stand up or if some motor was required to produce a torque exceeding 30 N/m, which was above the limit of a normal actuator. The results show a remarkably low failure rate of only 1.4 %. To further investigate the causes of the failures, we analyzed the unsuccessful cases and found that most occurred when the two rods nearly overlapped with each other. In theory, a complete overlap leads to a singular configuration, wherein the elastic cables align toward the robot's CoM, making the system uncontrollable. In practical situations, however, such a perfect overlap is unlikely to occur.

IV. EXPERIMENT

To examine the practical applicability of the legged-rolling locomotion to real robot, physical experiments were conducted using a prototype model. The prototype (Fig. 7(a)) consisted of two frames (each 0.5 m and 1.3 kg). The frames were interconnected with linear bearings, enabling rotational movement in the XOZ plane, while restricting Y-directional motion (Fig. 7(b)). The control system (Fig. 7(g)) included four brushless motors with integrated reducers and Hall sensors (ECXSP19M BL KL A STD 24V, and GPX22 C 62:1, Maxon, Switzerland), four motor drivers (EPOS4 Compact 50/5, Maxon, Switzerland), and a controller (PC software, self-developed) connected via USB. The actuation components (Fig. 7(c)) consisted of the above-mentioned motor and a 0.02

IEEE Robotics and Automation Letters (RA-L) paper, presented at ICRA 2026, Vienna, Austria. Cite as RA-L paper.

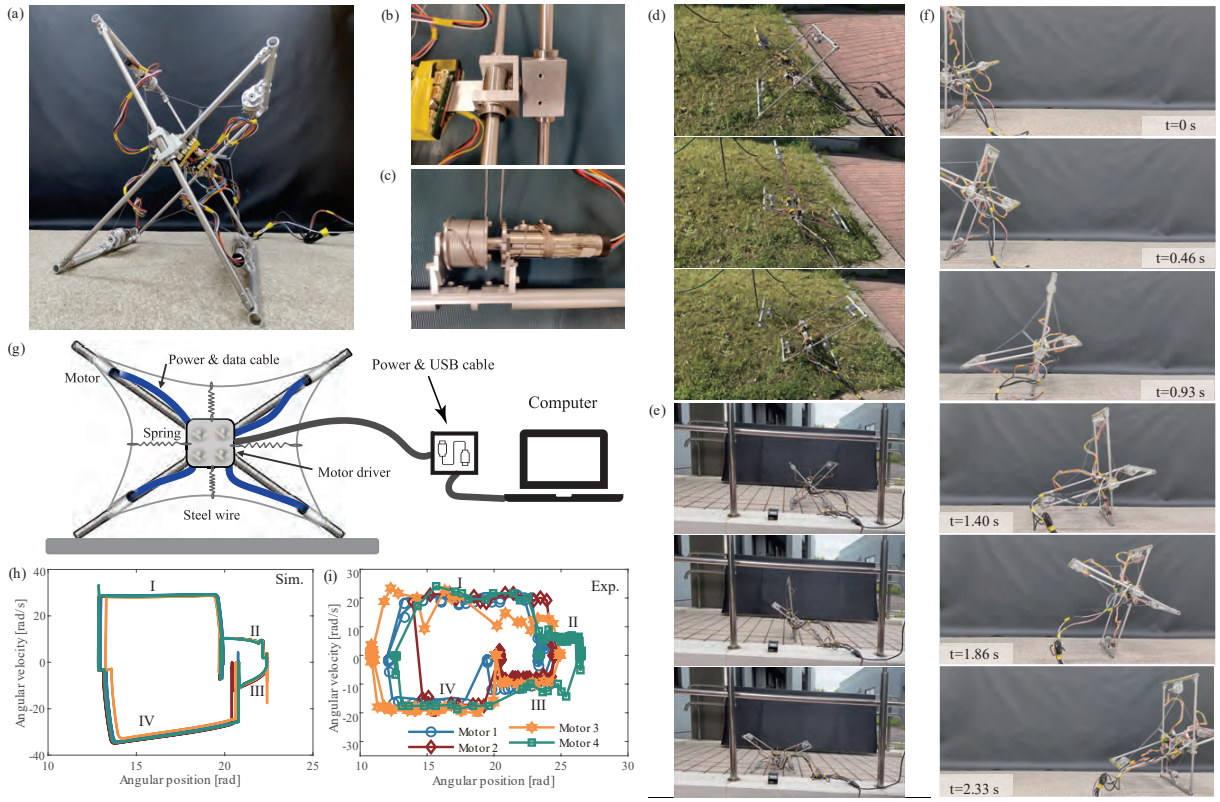

Fig. 7. (a) Two-frame robot. (b) Linear bearings enabling XOZ-rotation. (c) Actuation system composed of motor, gearbox, and a 0.02 m winder. (d,e) Outdoor quasi-static locomotion across varying terrains, including uphill and stair climbing. (f) Animated images of dynamic gait. (g) Control system composed of Maxon motors, EPOS4 drivers, and USB-connected computer. (h,i) Phase diagrams of four motors showing a limit cycle gait in simulation and experiment.

m radius winder (aluminum alloy, self-designed) with internal springs enhancing the system's elasticity. The specific control parameters for achieving dynamic gaits were set as follows.

- Phase 1: Hold the posture.
- Phase 2: $l_a(T_2) = 0.4(L-2l)/2$, $l_b(T_2) = 0.6(L-2l)/2$, $\theta(T_2) = 110\pi/180$, $T_2 = 0.4$.

As explored in the simulated dynamic gait (Fig. 5(b)), a simplified control was used, in which the posture was unchanged during phase 1. Also, to account for the real motor properties, the tracking postures for $l_a(T_2)$ and $l_b(T_2)$ were slightly adjusted.

To start a dynamic gait, the initial velocity should be set to nonzero. To provide an initial velocity, a slight push was applied to the robot at the beginning of the experiment. Fig. 7(f) shows snapshots of dynamic legged-rolling locomotion observed in the physical experiment with a time interval of 0.46 s. Fig. 7(i) represents a phase diagram $(\theta, \dot{\theta})$ of the four motors with a sampling time interval of 30 ms. It can be seen that a stable limit cycle was generated. The four labels (I, II, III, IV) indicate the four steps, each of which is completed when one of the four feet lands on the ground. Fig. 7(h) shows the corresponding simulation result, where the parameter values were set to be the same as those of the physical experiment, *i.e.*, (m, L, l)=(1.3, 0.5, 0.1). Although the simulated trajectory slightly deviated from the experiment, the general trend, such as the limit cycle gait visiting all four stages of I-IV, was reproduced quite well.

Finally, quasi-static gaits were performed experimentally to evaluate the robot's capability of traversing discrete terrains. The control parameters for phase 1 were set to $l_a(T_1) = 0.8(L-2l), l_b(T_1) = 0.1(L-2l), \theta(T_1) = 70\pi/180, T_1 = 0.4$. In phase 2, the current posture was maintained. At the end of each step, the robot performed a posture adjustment to return to the initial state before executing the next step. It was confirmed that the robot overcame discrete steps up to the height of 12±0.5 cm, which corresponds to more than 20 % of its frame length (refer to the accompanying video). Gaits with both long and short strides were also generated by varying the control parameters of phase 2 (long stride: $l_a(T_2) = 0.2(L-2l)$, $l_b(T_2) = 0.2(L-2l)$, $\theta(T_2) = 70\pi/180$, $T_2 = 0.4$; short stride: $\theta(T_2) = 140\pi/180$). As shown in Fig. 7(d,e), additional experiments such as uphill walking and stair climbing have also been performed in outdoor environments. The recordings of these experiments can be found in the supplementary video. It should be noted in the video that some slippings took place during the quasi-static gait, causing a certain difference between the simulations and experiments.

V. CONCLUSIONS AND DISCUSSIONS

This study proposed an underactuated control method for a minimally structured tensegrity robot to generate legged-rolling locomotion. Both simulations and physical experiments demonstrated that the proposed system is capable of producing quasi-static and dynamic gaits, which realized stable locomotion on both even and uneven terrains. The robot could also stand up autonomously from arbitrary states, achieving the self-recovery capability.

IEEE Robotics and Automation Letters (RA-L) paper, presented at ICRA 2026, Vienna, Austria. Cite as RA-L paper.

TABLE II
COMPARISON OF THE PROPOSED SYSTEM WITH OTHER ROBOTS.

Robots	Torso	Structural Complexity	Control Complexity	Applicable Terrain	Initial Posture Req.
Commercial Platform					
Unitree B2 [22]	Y	H	H	GD	N
Atlas [8]	Y	H	H	GD	Y
Legged-Rolling (Rigid)					
E-Paddle Mechanism [23]	Y	M	M	GD	N
Rimless Wheel [24], [25]	Y	L	L	SD	N
Legged-Rolling (Tensegrity)					
SUPERball v2 [26], [27]	N	M	H	C	N
Shape-Changing Robot [28]	Y	M	M	SD	N
Proposed Robot	N	L	L	GD	N

Symbol Definitions:
Y: Yes, N: No, H: High, M: Medium, L: Low.
GD: General Discrete, SD: Special Discrete (landing points constrained, *e.g.*, to stairs), C: Continuous.

To highlight the key features of the present study, Table II compares the proposed system with the representative robots in the light of: 1) presence of a torso, 2) structural complexity, 3) control complexity, 4) applicable terrain types, and 5) requirement on a specific initial condition (*i.e.*, whether specifically designed initial configuration is required to start locomotion). The proposed system is advantageous with low structural complexity (*i.e.*, two rods without a torso), low control complexity (*i.e.*, simple PD control), applicability to general discrete terrain, and no requirement on initiate conditions. Concerning the range of applicable terrains, commercial platforms such as Unitree B2 or Atlas possess a strong capability of moving on a very critical environment (*e.g.*, undeveloped or human-inaccessible environments), to which applicability of the present system might be limited. One of the reasons is because the present system is in the stage of fundamental research, which primarily focused on implementing and verifying the basic idea of legged-rolling locomotion. Because of the minimal design, the present tensegrity system is also restricted to planar locomotion, whereas most other robots in Table II move in a three-dimensional space. Future investigation should extend the system to locomote in a three-dimensional space and moreover to be applicable to more critical environments.

REFERENCES

[1] R. Siegwart, I. R. Nourbakhsh, and D. Scaramuzza, *Introduction to autonomous mobile robots*. MIT press, 2011.

[2] C. Liu, D. Wang, and Q. Chen, "Central pattern generator inspired control for adaptive walking of biped robots," *IEEE Transactions on Systems, Man, and Cybernetics: Systems*, vol. 43, no. 5, pp. 1206–1215, 2013.

[3] C. Yang, C. Pu, G. Xin, J. Zhang, and Z. Li, "Learning complex motor skills for legged robot fall recovery," *IEEE Robotics and Automation Letters*, vol. 8, no. 7, pp. 4307–4314, 2023.

[4] R. H. Armour and J. F. Vincent, "Rolling in nature and robotics: A review," *Journal of Bionic Engineering*, vol. 3, no. 4, pp. 195–208, 2006.

[5] H.-T. Lin, G. G. Leisk, and B. Trimmer, "Goqbot: a caterpillar-inspired soft-bodied rolling robot," *Bioinspiration & biomimetics*, vol. 6, no. 2, p. 026007, 2011.

[6] P. Holmes, R. J. Full, D. Koditschek, and J. Guckenheimer, "The dynamics of legged locomotion: Models, analyses, and challenges," *SIAM review*, vol. 48, no. 2, pp. 207–304, 2006.

[7] M. H. Raibert, *Legged robots that balance*. MIT press, 1986.

[8] S. Kuindersma, R. Deits, M. Fallon, A. Valenzuela, H. Dai, F. Permenter, T. Koolen, P. Marion, and R. Tedrake, "Optimization-based locomotion planning, estimation, and control design for the atlas humanoid robot," *Autonomous robots*, vol. 40, pp. 429–455, 2016.

[9] J. Laumond, M. Benallegue, J. Carpentier, and A. Berthoz, "The yoyo-man," *The International Journal of Robotics Research*, vol. 36, no. 13-14, pp. 1508–1520, 2017.

[10] S.-C. Chen, K.-J. Huang, W.-H. Chen, S.-Y. Shen, C.-H. Li, and P.-C. Lin, "Quattroped: A leg–wheel transformable robot," *IEEE/ASME Transactions on Mechatronics*, vol. 19, no. 2, pp. 730–742, 2014.

[11] M. Bjelonic, P. K. Sankar, C. D. Bellicoso, H. Vallery, and M. Hutter, "Rolling in the deep–hybrid locomotion for wheeled-legged robots using online trajectory optimization," *IEEE Robotics and Automation Letters*, vol. 5, no. 2, pp. 3626–3633, 2020.

[12] G. Quaglia, D. Maffiodo, W. Franco, S. Appendino, and R. Oderio, "The epi. q-1 hybrid mobile robot," *The International Journal of Robotics Research*, vol. 29, no. 1, pp. 81–91, 2010.

[13] I. Fantoni and R. Lozano, *Non-linear control for underactuated mechanical systems*. Springer Science & Business Media, 2002.

[14] J. Zhang and M. Ohsaki, *Tensegrity structures*. Springer, 2015, vol. 7.

[15] Y. Zheng, F. Asano, C. Yan, L. Li, and I. T. Tokuda, "Tensegrity-based legged robot generates passive walking, skipping, and crawling gaits in accordance with environment," *IEEE/ASME Transactions on Mechatronics*, 2025.

[16] C. Paul, F. J. Valero-Cuevas, and H. Lipson, "Design and control of tensegrity robots for locomotion," *IEEE Transactions on Robotics*, vol. 22, no. 5, pp. 944–957, 2006.

[17] Z. Mao, R. Kobayashi, H. Nabae, and K. Suzumori, "Multimodal strain sensing system for shape recognition of tensegrity structures by combining traditional regression and deep learning approaches," *IEEE Robotics and Automation Letters*, vol. 9, no. 11, pp. 10 050–10 056, 2024.

[18] Y. Zheng, L. Li, F. Asano, C. Yan, X. Zhao, and H. Chen, "Modeling and analysis of tensegrity robot for passive dynamic walking," *2021 IEEE/RSJ International Conference on Intelligent Robots and Systems (IROS)*, pp. 2479–2484, 2021.

[19] Y. Zheng, L. Li, and S. Ma, "Legged locomotion control of an under-actuated eccentric paddle mechanism with torso stabilization," *2023 IEEE/RSJ International Conference on Intelligent Robots and Systems (IROS)*, pp. 4293–4298, 2023.

[20] J. C. Larsen and K. Stoy, "Energy efficiency of robot locomotion increases proportional to weight," *Procedia Computer Science*, vol. 7, pp. 228–230, 2011, proceedings of the 2nd European Future Technologies Conference and Exhibition 2011 (FET 11).

[21] A. Kuo, "Choosing your steps carefully," *IEEE Robotics & Automation Magazine*, vol. 14, no. 2, pp. 18–29, 2007.

[22] U. Robotics, "B2: Go beyond the limits," https://m.unitree.com/b2/.

[23] Y. Sun and S. Ma, "epaddle mechanism: Towards the development of a versatile amphibious locomotion mechanism," *2011 IEEE/RSJ International Conference on Intelligent Robots and Systems*, pp. 5035–5040, 2011.

[24] K. Shankar and J. W. Burdick, "Motion planning and control for a tethered, rimless wheel differential drive vehicle," *2013 IEEE/RSJ International Conference on Intelligent Robots and Systems*, pp. 4829–4836, 2013.

[25] Y. Hanazawa, "Development of rimless wheel with controlled wobbling mass," *2018 IEEE/RSJ International Conference on Intelligent Robots and Systems (IROS)*, pp. 4333–4339, 2018.

[26] M. Vespignani, J. M. Friesen, V. SunSpiral, and J. Bruce, "Design of superball v2, a compliant tensegrity robot for absorbing large impacts," *2018 IEEE/RSJ International Conference on Intelligent Robots and Systems (IROS)*, pp. 2865–2871, 2018.

[27] M. Vespignani, C. Ercolani, J. M. Friesen, and J. Bruce, "Steerable locomotion controller for six-strut icosahedral tensegrity robots," *2018 IEEE/RSJ International Conference on Intelligent Robots and Systems (IROS)*, pp. 2886–2892, 2018.

[28] S. Spiegel, J. Sun, and J. Zhao, "A shape-changing wheeling and jumping robot using tensegrity wheels and bistable mechanism," *IEEE/ASME Transactions on Mechatronics*, vol. 28, no. 4, pp. 2073–2082, 2023.